Controllable Metamaterial-Loaded Waveguides Supporting Backward and Forward Waves

Fan-Yi Meng, *Member, IEEE*, Qun Wu, *Senior Member, IEEE*, Daniel Erni, *Member, IEEE*, and Le-Wei Li, *Fellow, IEEE*

***Abstract*—Rectangular waveguides loaded by anisotropic metamaterials are analyzed to assess the controllability of transmission characteristics of the involved electromagnetic waves. Dispersion relations of $\mathrm{TE}_{\mathrm{m0}}$ modes in the metamaterial-loaded waveguide (MLW) are theoretically investigated. It is shown that all propagating modes (the forward wave, the backward wave and the evanescent wave) in the MLW can be realized below the cut-off frequency by changing transverse and longitudinal components of permeability tensors of the loading metamaterials. Numerical simulations are carried out to verify the proposed theory and the controllability. Transmission characteristics and effective constitutive parameters of three MLWs with different cells, which should theoretically support forward waves, backward waves and evanescent waves, respectively, are numerically calculated. Dispersion curves and magnetic field distribution for the backward wave MLW and the forward wave MLW are simulated. It is shown that the simulated results are in a good agreement with theoretical predictions. Implementation of the controllable MLW was achieved by using axially rotating control rods. Rotating the control rods can reconfigure the metamaterial and make propagating modes in the MLW switch from backward waves to forward waves or evanescent waves.**

***Index Terms*—Backward wave, controllability, evanescent wave, forward wave, metamaterial-loaded waveguide.**

I. Introduction

RECTANGULAR waveguides are commonly used as basic guiding structures in microwave, radar and antenna technology. Moreover, there are many applications of the waveguide as radiating elements. The most familiar example is a slotted waveguide antenna, which is popular in navigation, radar and other high-frequency systems. It has a high efficiency and supports linear polarization with low cross-polarization. Such an antenna is often used in aircraft applications because it can be made to conform to the surface on which it is mounted. A leaky-wave antenna is basically also a waveguide structure that possesses a controllable mechanism for power leakage all along its length. The radiated beam of the leaky wave antenna may be frequency scannable, producing a fan beam that is narrow in the scan plane. The frequency scannable leaky wave antennas are cost effective in systems like low cost radars, side looking sensors in vehicles and imaging because phase shifters and associated circuit elements are not required to provide the beam steering [1].

Recently, a very unusual rectangular waveguide was proposed by Marques *et al.* in [2], [3] and then extensively studied by Hrabar *et al.* in [4]–[6]. The rectangular metallic waveguide is loaded with split ring resonators (SRRs) [7]–[11], which have the property of negative permeability and are also used to realize the left-handed metamaterial (LHM) along a composite with both, negative permittivity and permeability [12]–[17]. The metamaterial loaded waveguide (MLW) supports the propagation of backward waves below the cut-off frequency of the hollow waveguide [18]. The MLW has attracted extensive attention [19]–[32] since it provides an alternative approach for the realization of negative index metamaterials as well as a unique method for the miniaturization of waveguide-based devices. Hrabar *et al.* [4] showed that backward propagation occurs when the longitudinal permeability is positive and the transversal permeability is negative and that a MLW with broad bandwidth can be realized by proper feedings. Eshrah *et al.* [28], [29] designed and fabricated a sub-wavelength rectangular waveguide with dielectric-filled corrugations supporting backward waves. Belov *et al.* [33] theoretically studied rectangular metallic waveguides that are periodically loaded with uniaxial resonant scatterers based on the local field approach (i.e. the dipole approximation). Xu *et al.* [23] performed experiments and simulations to study the transmission of electromagnetic waves through waveguides loaded by resonance structures of electric and magnetic type.

It is worth mentioning that in case of a metamaterial with anisotropic unit cells the electromagnetic characteristics of the metamaterial can be effectively tuned simply by changing the arrangement of unit cells. Hence, when integrated in a rectangular waveguide the tunability of the metamaterial enables the waveguide to provide the further advantage of controllable transmis-

Manuscript received April 01, 2010; revised December 07, 2010; accepted February 09, 2011. Date of publication July 12, 2011; date of current version September 02, 2011. This work was supported in part by the National Natural Science Foundation of China under Grants 60801015 and 60971064, the Open Project Program of the State Key Laboratory of Millimeter Wave under Grants K201007 and K201006, the Development Program for Outstanding Young Teachers in Harbin Institute of Technology under Grant HITQNJS.2008.07, the Fundamental Research Funds for the Central Universities under Grant HIT.IBRSEM.2009, and in part by the Aviation Science Funds under Grant 20080177013.

F.-Y. Meng and Q. Wu are with the Department of Microwave Engineering, Harbin Institute of Technology, Harbin 150001, China, and also with the State Key Laboratory of Millimeter Waves, Nanjing 210096, China (e-mail: blade@hit.edu.cn; qwu@hit.edu.cn).

D. Erni is with the Laboratory for General and Theoretical Electrical Engineering (ATE), Faculty of Engineering, University of Duisburg-Essen, and CeNIDE-Center for Nanointegration Duisburg-Essen, D-47048 Duisburg, Germany (e-mail: daniel.erni@uni-due.de).

L.-W. Li is with Department of Electrical and Computer Engineering, National University of Singapore, Kent Ridge 119260, Singapore (e-mail: lwli@nus.edu.sg).

Color versions of one or more of the figures in this paper are available online at http://ieeexplore.ieee.org.

Digital Object Identifier 10.1109/TAP.2011.2161540

sion characteristics, in addition to the smaller waveguide cross section.

Making rectangular waveguides controllable so that their behavior may adapt to changing system requirements or environmental conditions can ameliorate or eliminate restrictions and provide additional functionality on the system level. For example, the controllability of the propagating rectangular waveguide mode can give rise to leaky wave antennas with fixed frequency scannability. In fact, the fixed frequency scannability is often preferable to frequency scannability in certain applications where a narrow frequency band is available and wide angle of coverage is required. Such controllable waveguides can also help to broaden the scanning range of leaky wave antennas, which increases link capacity of e.g. multiple input multiple output (MIMO) communication systems [34]–[37].

In this paper, we focus on the effects emerging from corresponding changes in the position and direction of the loading metamaterial cells in MLWs. Transmission characteristics of electromagnetic waves in the MLWs are theoretically analyzed. Moreover, numerical simulations are performed to demonstrate the controllability of the MLWs. The work done in this paper is of practical relevance in designing controllable MLWs and corresponding tunable microwave and RF devices.

II. Theory Description

Consider a z-directional rectangular waveguide whose width and height are denoted by a and b, respectively, as shown in Fig. 1. The walls of the waveguide are perfect electric conductors (PEC). The waveguide is loaded with lossless anisotropic metamaterial having the following permeability tensor and permittivity

$$\bar{\mu} = \mu_0 \begin{bmatrix} \mu_x & 0 & 0 \\ 0 & \mu_y & 0 \\ 0 & 0 & \mu_z \end{bmatrix} = \mu_0 \bar{\mu}_r$$
$$\varepsilon = \varepsilon_0 \varepsilon_r. \tag{1}$$

The field distribution inside the waveguide satisfies source-free curl Maxwell equations

$$\nabla \times \vec{E} = -j\omega\mu_0 \bar{\mu}_r \vec{H}, \tag{2}$$
$$\nabla \times \vec{H} = j\omega\varepsilon_0 \varepsilon_r \vec{E}. \tag{3}$$

Assuming $\vec{E}(x,y,z) = \vec{E}(x,y)e^{-\gamma z}$ and $\vec{H}(x,y,z) = \vec{H}(x,y)e^{-\gamma z}$, following relation can be derived from (2) and (3) for TE modes

$$H_x = -\frac{\gamma}{\gamma^2 + k_0^2 \mu_x \varepsilon_r} \frac{\partial H_z}{\partial x}$$
$$H_y = -\frac{\gamma}{\gamma^2 + k_0^2 \mu_y \varepsilon_r} \frac{\partial H_z}{\partial y}. \tag{4}$$

On the other hand, inserting (3) into (2) leads to the vector wave equation for the electric field

$$\nabla \times (\nabla \times \vec{H}) = k_0^2 \bar{\mu} \varepsilon \vec{H}. \tag{5}$$

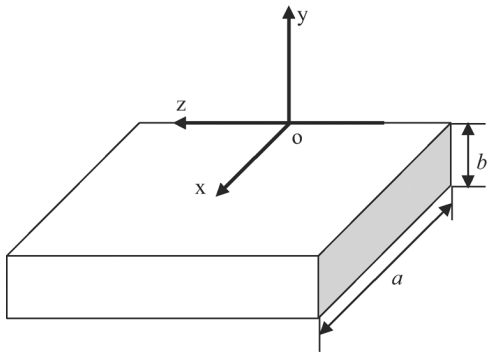

Fig. 1. Outline of the rectangular waveguide with cross-section $a \times b$. The waveguide is loaded with metamaterial along the z-direction.

From (5) the quantity equation for the z-component is obtained as

$$-\frac{\partial^2 H_z}{\partial x^2} - \frac{\partial^2 H_z}{\partial y^2} + \frac{\partial^2 H_x}{\partial x \partial z} + \frac{\partial^2 H_y}{\partial y \partial z} = k_0^2 \mu_z \varepsilon_r H_z. \tag{6}$$

Inserting (4) into (6) leads to

$$\frac{k_0^2 \mu_x}{\gamma^2 + k_0^2 \mu_x \varepsilon_r} \frac{\partial^2 H_z}{\partial x^2} + \frac{k_0^2 \mu_y}{\gamma^2 + k_0^2 \mu_y \varepsilon_r} \frac{\partial^2 H_z}{\partial y^2} + k_0^2 \mu_z H_z = 0. \tag{7}$$

Solving this differential equation yields the dispersion equation for the rectangular waveguide loaded with anisotropic metamaterial

$$\frac{\mu_x}{k_0^2 \mu_x \varepsilon_r - k_z^2} \left(\frac{m\pi}{a}\right)^2 + \frac{\mu_y}{k_0^2 \mu_y \varepsilon_r - k_z^2} \left(\frac{n\pi}{b}\right)^2 = \mu_z. \tag{8}$$

From (8) one finds the expression for the propagation factor

$$k_z^2 = \frac{1}{2} \left\{ k_0^2 \varepsilon_r (\mu_x + \mu_y) - k_x^2 \frac{\mu_x}{\mu_z} - k_y^2 \frac{\mu_y}{\mu_z} \pm \sqrt{\left[k_0^2 \varepsilon_r (\mu_x - \mu_y) - k_x^2 \frac{\mu_x}{\mu_z} + k_y^2 \frac{\mu_y}{\mu_z} \right]^2 + 4 k_x^2 k_y^2 \frac{\mu_y \mu_x}{\mu_z^2}} \right\}$$
$$k_x = \frac{m\pi}{a}, k_y = \frac{n\pi}{b}. \tag{9}$$

For $\mathrm{TE_{m0}}$ modes, the dispersion relation (9) is simplified to

$$k_z^2 = k_0^2 \varepsilon_r \mu_x - \frac{\mu_x}{\mu_z} \left(\frac{m\pi}{a}\right)^2 \tag{10}$$

On the other hand, corresponding calculations show that the wave impedance of $\mathrm{TE_{m0}}$ is given by

$$\eta^2 = \frac{\eta_0^2 \mu_x}{\varepsilon_y \left(1 - \frac{1}{\varepsilon_y \mu_z} \left(\frac{m\pi}{a k_0}\right)^2\right)}. \tag{11}$$

Let us consider a homogeneous medium with effective permittivity $\varepsilon_{\mathrm{eff}}$ and permeability μ_{eff}. For a plane EM wave propagating along the z direction inside the medium, the dispersion

relation and the wave impedance are

$$k_z^2 = k_0^2 \varepsilon_{\text{eff}} \mu_{\text{eff}}$$
$$\eta^2 = \eta_0^2 \mu_{\text{eff}} / \varepsilon_{\text{eff}}. \tag{12}$$

The comparison between (10), (11) and (12) suggests that the MLW can be viewed as an effective medium with [2], [3]

$$\varepsilon_{\text{eff}} = \varepsilon_r \left(1 - \frac{1}{\varepsilon_r \mu_z} \left(\frac{m\pi}{ak_0}\right)^2\right)$$
$$\mu_{\text{eff}} = \mu_x. \tag{13}$$

Moreover, there is

$$k_z = \begin{cases} k_0 \sqrt{\varepsilon_{\text{eff}} \mu_{\text{eff}}}, & \text{Re}[\varepsilon_{\text{eff}}] > 0 \text{ and } \text{Re}[\mu_{\text{eff}}] > 0 \\ -k_0 \sqrt{\varepsilon_{\text{eff}} \mu_{\text{eff}}}, & \text{Re}[\varepsilon_{\text{eff}}] < 0 \text{ and } \text{Re}[\mu_{\text{eff}}] < 0 \\ -jk_0 \sqrt{\varepsilon_{\text{eff}} \mu_{\text{eff}}}, & \text{Re}[\varepsilon_{\text{eff}}] * \text{Re}[\mu_{\text{eff}}] < 0. \end{cases} \tag{14}$$

Transmission characteristics of MLWs in the case of $\text{Re}[\mu_z] > 0$ have been analyzed and discussed in detail in [4]. It has been shown that MLWs with $\text{Re}[\mu_z] > 0$ and $\text{Re}[\mu_x] < 0$ support backward wave propagation below the cut-off frequency of the corresponding empty waveguide. Here, we focus on the case of $\text{Re}[\mu_z] < 0$, where from (13) one can setup the following relation

$$\text{Re}[\varepsilon_{\text{eff}}] = \text{Re}[\varepsilon_r] - \text{Re}\left[\frac{1}{\mu_z}\right] \left(\frac{m\pi}{ak_0}\right)^2$$
$$\text{Re}[\varepsilon_{\text{eff}}] > \text{Re}[\varepsilon_r] > 0. \tag{15}$$

This means that $\text{Re}[\varepsilon_{\text{eff}}]$ is positive at any frequency. Therefore, considering $\mu_{\text{eff}} = \mu_x$, it can be inferred that MLWs with $\text{Re}[\mu_x] > 0$ and $\text{Re}[\mu_z] < 0$ support propagation of forward waves, whereas MLWs with $\text{Re}[\mu_x] < 0$ and $\text{Re}[\mu_z] < 0$ yields exponentially attenuated waves, irrespective of whether the operating frequency is above or below the cut-off frequency of the empty waveguide.

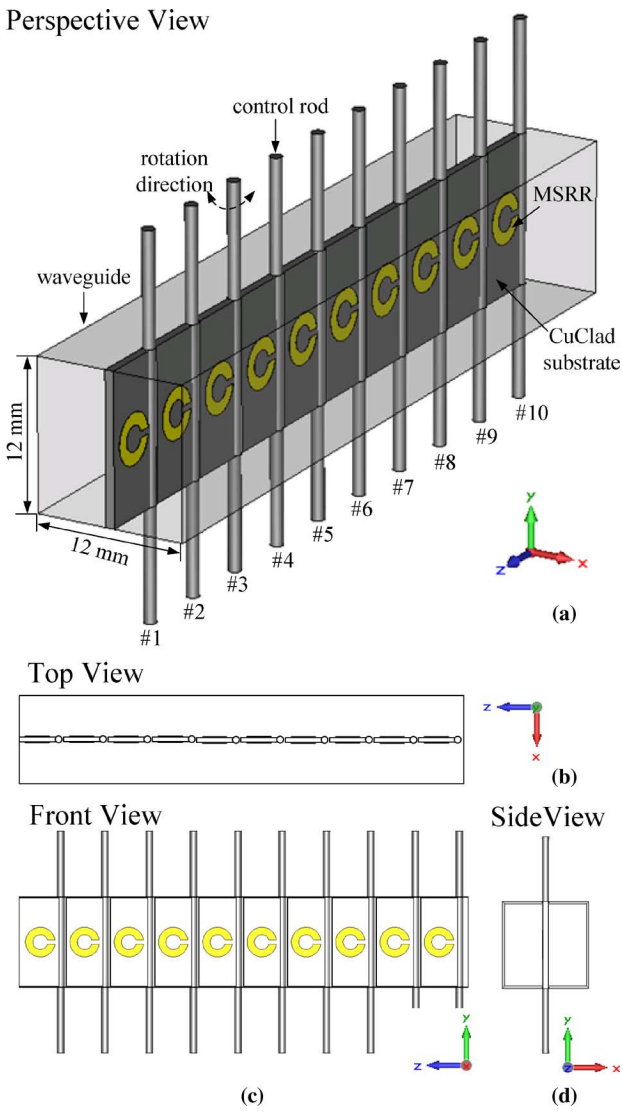

Fig. 2. Geometry of the controllable MLW in the case of backward wave. (a) The perspective view. (b) The top view. (c) The front view. (d) The side view.

III. Controllable MLWS

According to the analysis in the above section, it is now known that propagating modes of MLWs can be controlled by changing the permeability tensors of the underlying metamaterials. Thus, controllable MLWs can be realized. A possible scheme for the implementation of controllable MLWs is shown in Fig. 2. The controllable MLW is set up as a conventional waveguide loaded with a metamaterial which consists of an array of disconnected modified split ring resonators (MSRRs) [38], [cf. Fig. 3(a) and 3(b) (inset)]. The MSRR has much higher mutual capacitance between the rings compared to the ordinary SRR. Therefore, it can lower the resonance frequency and allow the fabrication of inclusions of smaller "electrical dimensions", which are defined as the ratio of physical dimensions to the operating wavelength. In addition, the MSRR can suppress the unwanted bianisotropic effects [4], [38].

Each metamaterial cell (MSRR) is attached to an axially rotating dielectric control rod that is vertically fixed through holes in the upper and lower wall of the waveguide. Control rods are periodically arranged along the z-directional line of symmetry of the waveguide. Thus, as these control rods are rotated, the metamaterial cells are rotated too, which changes the permeability tensor of the loading metamaterial in the MLW because of the varying anisotropy of the MSRR. Consequently, the controllability of the MLW is carried out this way. For example, if the odd-numbered rods (#1, 3, 5, 7, and 9) in Fig. 2(a) are turned anti-clockwise by 90° and the even-numbered rods (#2, 4, 6, 8, and 10) are turned clockwise by 90°, the MLW as shown in Fig. 14 is realized. If only the odd-numbered rods in Fig. 2(a) undergo a clockwise rotation by 90° and the even-numbered rods are kept unchanged, the MLW yields a structure as shown in Fig. 20. In this study, physical parameters of the MSRR have been extracted from an experimental analysis in [4]. The MSRR comprises two copper rings placed back to back on CuClad substrate (substrate thickness 0.7 mm, $\varepsilon_r = 2.6$) with slots oriented in opposite directions. The rings have an outer diameter of 4 mm with track width of 1 mm and a slit width of 0.5 mm. In addition, the waveguide has a cross-section of 12 mm × 12 mm and a cut-off frequency of 12.5 GHz. In the following section, the electromagnetic properties of the MSRR are investigated.

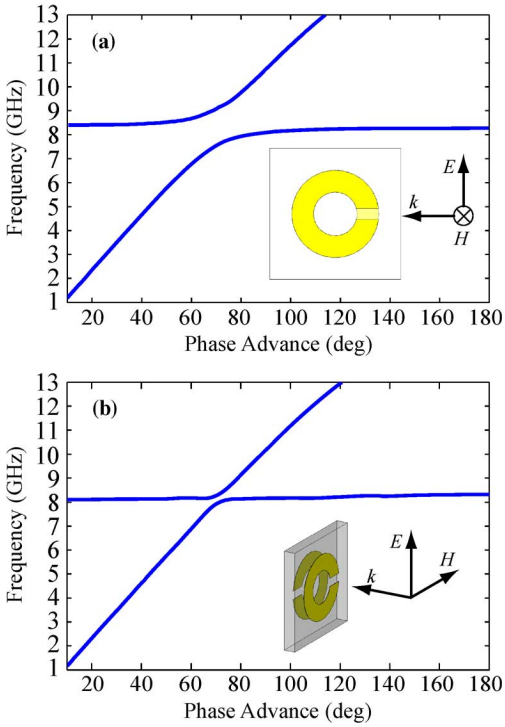

Fig. 3. (a) Dispersion curve for the parallel polarization $H_{||}$. (b) Dispersion curve for the perpendicular polarization $H_{\perp}$.

Using HFSS, a commercial electromagnetic software package based on the finite-element method (FEM), dispersion curves are computed for an infinite periodic array of the MSRRs with the thickness of one unit cell. There are two incident polarizations of interest: magnetic field polarized along the split ring axes [$H_{||}$, cf. inset of Fig. 3(a)], and perpendicular to the split ring axes [$H_{\perp}$, cf. inset of Fig. 3(b)]. In both cases, the electric field is in the plane of the rings. As shown by the curves in Fig. 3(a) and 3(b), a band gap is found in either case. We will show that the $H_{||}$ gap is due to negative effective permeability μ_{eff} while the $H_{\perp}$ gap is due to a small resonance, which causes neither negative effective permeability μ_{eff} nor negative effective permittivity ε_{eff}.

Effective constitutive parameters μ_{eff} and ε_{eff} of the MSRR metamaterial are extracted from transmission and reflection data. Similar to [39], our extraction approach also begins by introducing the composite terms V_1 and V_2 with S-parameters

$$\begin{aligned} V_1 &= s_{21} + s_{11} \\ V_2 &= s_{21} - s_{11} \end{aligned} \tag{16}$$

and deriving following quantities [39]

$$X = \frac{1 + V_1 V_2}{V_1 + V_2} = \frac{1 + Z^2}{2Z} \tag{17}$$

where the transmission term

$$Z = \exp(-j\omega k_0 \sqrt{\mu_{\text{eff}} \varepsilon_{\text{eff}}}\, d). \tag{18}$$

Consequently, from (17) one obtains

$$Z = X \pm \sqrt{X^2 - 1}. \tag{19}$$

Note that the expression for Z is a complex function with multiple branches. The ambiguity can be resolved using the condition $\text{Re}[\eta_{\text{eff}}] > 0$. The combination of (18) and (19) yields

$$\sqrt{\mu_{\text{eff}} \varepsilon_{\text{eff}}} = j \frac{\ln(Z)}{\omega k_0 d}. \tag{20}$$

In the same sense one gets the following exact expression [39]

$$\eta_{\text{eff}} = \eta_0 \frac{1 + Z}{1 - Z} \frac{1 - V_2}{1 + V_2} = \eta_0 \sqrt{\mu_{\text{eff}} / \varepsilon_{\text{eff}}}. \tag{21}$$

Combining (20) and (21) yields the closed-form relation for the effective permeability μ_{eff} and the effective permittivity ε_{eff}

$$\mu_{\text{eff}} = j \frac{\ln(Z)}{\omega k_0 d} \frac{1 + Z}{1 - Z} \frac{1 - V_2}{1 + V_2} \tag{22}$$

$$\varepsilon_{\text{eff}} = j \frac{\ln(Z)}{\omega k_0 d} \frac{1 - Z}{1 + Z} \frac{1 + V_2}{1 - V_2}. \tag{23}$$

The expressions for μ_{eff} and ε_{eff} are equivalent to those in [40], [41], but their calculation procedures are different. We use this extraction approach because the condition $\text{Re}[\eta_{\text{eff}}] > 0$ in such a calculation can help to effectively select the correct branch in the expressions for μ_{eff} and ε_{eff} for all reported cases in this paper.

An incident plane wave with $H_{||}$ polarization is necessary to calculate the S-parameters for the extraction of the effective permeability tensor component along the split ring axes [$\mu_{\text{eff}||}$] while an incident plane wave with $H_{\perp}$ is required for the extraction of the effective permeability tensor component parallel to the split ring plane [$\mu_{\text{eff}\perp}$]. There are also other issues worth noting in the calculation of the S-parameters for extraction, which are elaborately discussed in [39]–[41]. Fig. 4(a) and (b) display the retrieval of $\mu_{\text{eff}||}$ and $\varepsilon_{\text{eff}||}$ for the incident wave according to the inset in Fig. 3(a), respectively. It can be observed that the real part of $\mu_{\text{eff}||}$ is negative near 8.35 GHz while the real part of $\varepsilon_{\text{eff}||}$ is positive. The oscillation in the $\varepsilon_{\text{eff}||}$ curves indicates that the MSRR provides not only a magnetic response, but also an electric one. It is worth mentioning that the imaginary part of $\mu_{\text{eff}\perp}$ is positive although the imaginary part of $\mu_{\text{eff}||}$ is negative. This seems nonphysical because imaginary parts of both the complex permeability and permittivity are always negative for conventional passive materials. However, such positive imaginary part is a common phenomenon for metamaterials. For example, the single-SRR-metamaterial in [42] and the SRR-metamaterial in [40] have positive $\text{Im}[\mu_{\text{eff}}]$ and negative $\text{Im}[\varepsilon_{\text{eff}}]$. Because [40] and [42] used the $e^{-j\omega t}$ convention to extract μ_{eff} and ε_{eff}, their positive $\text{Im}[\mu_{\text{eff}}]$ and negative $\text{Im}[\varepsilon_{\text{eff}}]$ have the same physical meaning with the negative $\text{Im}[\mu_{\text{eff}}]$ and the positive $\text{Im}[\varepsilon_{\text{eff}}]$ compared to our notation. We think that the positive $\text{Im}[\varepsilon_{\text{eff}}]$ shown in Fig. 4(b), which represents active materials, is closely related to radiation losses [43]. As stated in [43], the total loss leading to the negative $\text{Im}[\mu_{\text{eff}}]$ of SRR includes two principal components: radiation loss and dissipation loss. Moreover, radiation loss dominates and far exceeds dissipation loss, even in the optical regime, where ohmic losses are usually high. Radiation loss results from the electromagnetic energy that is scattered by the metamaterial elements away from the incident wave. Therefore, different from dissipation

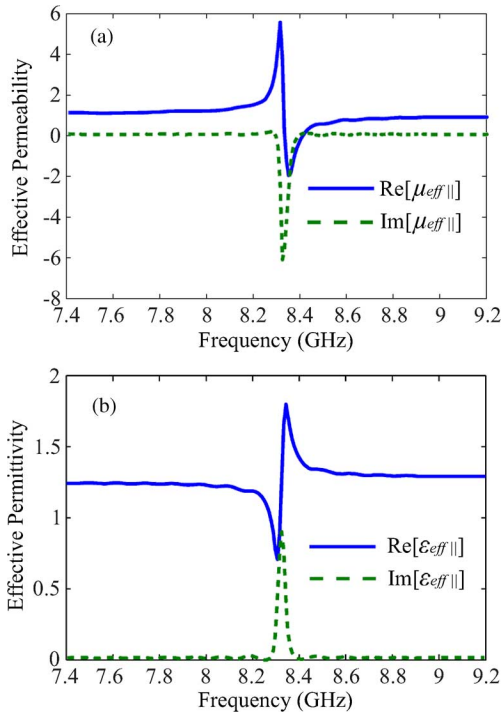

Fig. 4. Extracted real part and imaginary parts of (a) $\mu_{\text{eff}||}$ and (b) $\varepsilon_{\text{eff}||}$ of the MSRR metamaterial. The solid line represents the real part while the dashed line represents the imaginary part.

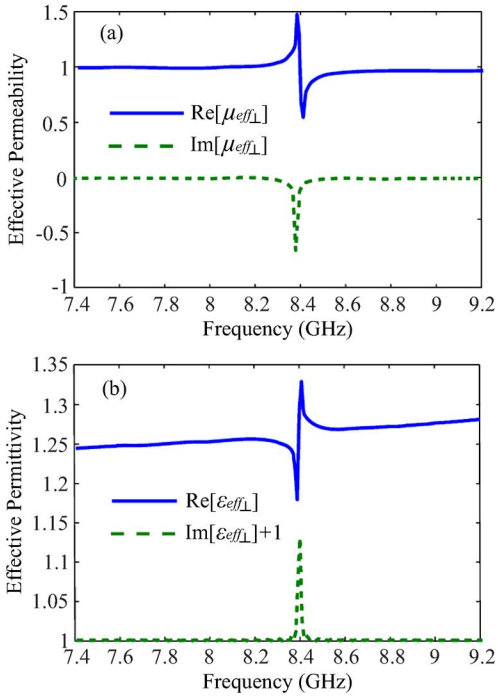

Fig. 5. Extracted real part and imaginary parts of (a) $\mu_{\text{eff}\perp}$ and (b) $\varepsilon_{\text{eff}\perp}$ of the MSRR metamaterial. The solid line represents the real part while the dashed line represents the imaginary part.

loss, radiation loss is not a real irreversible loss that is associated to the conversion of electromagnetic energy into other energy forms such as e.g. heat energy. Because of the conservation of electromagnetic energy, it can be inferred that the positive $\text{Im}[\varepsilon_{\text{eff}}]$ [Fig. 4(b)] should arise from the scattered electromagnetic wave, which causes the radiation loss and contributes to the negative $\text{Im}[\mu_{\text{eff}}]$ [Fig. 4(a)].

Fig. 5 shows the extracted $\mu_{\text{eff}\perp}$ together with the corresponding $\varepsilon_{\text{eff}\perp}$ for an incident wave that is polarized as displayed in the inset of Fig. 3(b). It can be seen that the real parts of $\mu_{\text{eff}\perp}$ and $\varepsilon_{ef\perp}$ are always positive, although there is a small resonance near 8.4 GHz. In addition, while comparing Fig. 4 with Fig. 5, it can be observed that for different incident waves, the resonance frequencies of the MSRR are slightly differing. The reason is that the dimension of the MSRR is not very small [about 0.18 **of the wavelength**], and thus the quasi-static equivalent circuit elements of the MSRR slightly change with respect to the different directions and forms of the incident wave.

Fig. 6 depicts the dispersion curves for the MSRR when the split ring axis of the MSRR encompasses angles of 15°, 30°, 45°, 60°, and 75° with respect to the magnetic field polarization direction. One finds that, as the angle increases, the width of the band gap reduces and the resonance of the MSRR weakens. A comparison between the dispersion curves in Fig. 6 and Fig. 3 reveals that the bandwidth of the $H_{||}$ gap for the angle of 0° is wider than those in the other cases, where the angle deviates from 0°. This means that the resonance of the MSRR is strongest when the magnetic field is polarized along the split ring axis. The influence of the rotation angle on the negative permeability effect of the MSRR is also worth investigating on its own. The

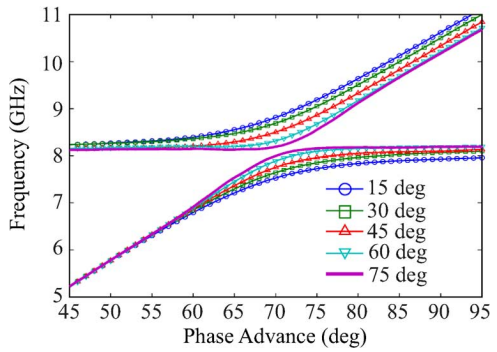

Fig. 6. Dispersion curves for the MSRR when split ring axis of the MSRR encompasses angles of 15°, 30°, 45°, 60°, and 75° to the polarization direction of the magnetic field. The line with circles corresponds to the angle of 15°. The line with squares corresponds to the angle of 30°. The line with up-triangles corresponds to the angle of 45°. The line with down-triangles corresponds to the angle of 60°. The thick line corresponds to the angle of 75°.

effective permeability of metamaterials consisting of MSRRs that are rotated by 30° and 50° with respect to the $H_{||}$ case is extracted and their real parts are shown in Fig. 7. The spectral responses feature a negative permeability (cf. negative peak) that still exists when the angle is 30° but tends to disappear when approaching 50°. The effective permeability of MSRR metamaterials, where the split ring axes encompass other polarization angles to the magnetic field, is also extracted although not shown here. It is observed that such metamaterials provide negative effective permeabilities when the angles are smaller than 50°.

The dispersion curve for a two-dimensional (2-D) metamaterial composed of crossed MSRRs [cf. Fig. 8 (inset)] is simulated and depicted in Fig. 8. It can be seen that the dispersion curve is very similar to the one shown in Fig. 3(a) because the effect

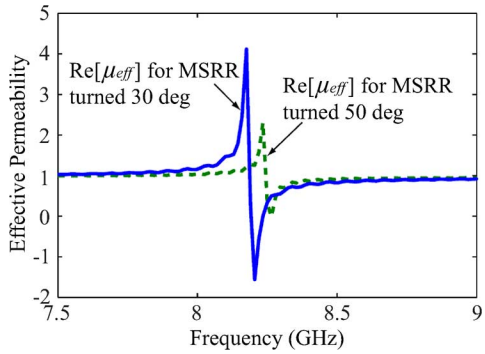

Fig. 7. Extracted real parts of the effective permeability of the metamaterials consisting of MSRRs turned 30° and 50° with respect to the $H_{||}$ case. The solid line corresponds to the MSRRs turned 30°. The dashed line corresponds to the MSRRs turned 50°.

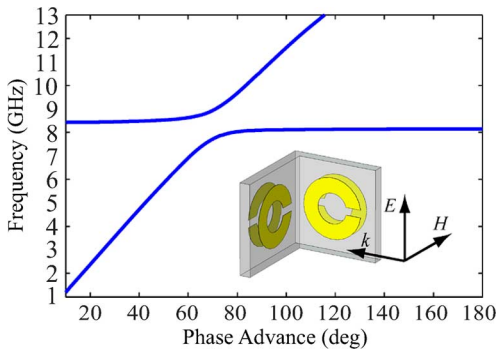

Fig. 8. Dispersion curve for two-dimensional (2-D) metamaterial composed of crossed MSRRs.

of the MSRR, whose split ring axis is perpendicular to the magnetic field polarization, on the electromagnetic characteristics of the 2-D metamaterial is weak. In addition, for the crossed MSRRs, there is also a quite narrow dispersion curve caused by the MSRR, whose split ring axis is perpendicular to the magnetic field polarization, although it is not shown here.

IV. Numerical Simulation

According to the analyses in Sections II and III, we have shown that as the control rods turn, the propagating mode field in the controllable MLW can be **either a forward, backward or evanescent wave**. Numerical simulations are performed to validate the controllability of the MLW in following three cases. Note that the effect of the control rods is not considered in this section but in the subsequent Sections V. Moreover, the material losses of copper associated to the MSRR structures are considered in all simulations in this paper.

Case A. Backward Wave MLW: In the case as shown in Fig. 2, the split rings axes are parallel to the x-direction, and the MSRR metamaterial provides a negative μ_x and a positive μ_z near 8.35 GHz because $\mu_x = \mu_{\text{eff}||}$ and $\mu_z = \mu_{\text{eff}\perp}$. Therefore, according to (13) and (14), the MLW will have a negative effective permittivity and a negative effective permeability to support the propagation of a backward wave near 8.35 GHz. Transmission characteristics of the MLW are simulated using CST MW STUDIO. Fig. 9 shows the corresponding simulation system. The MLW is

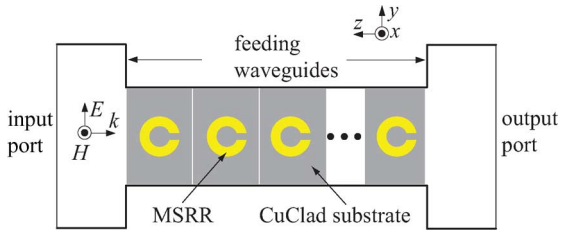

Fig. 9. Simulation system for the transmission characteristics of the backward wave MLW.

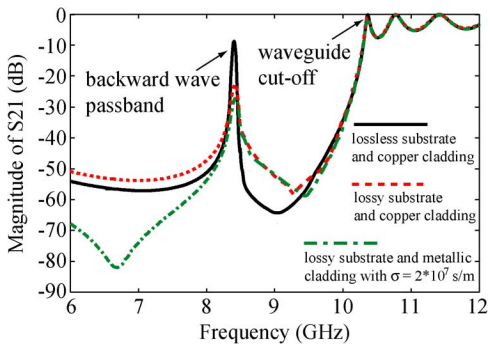

Fig. 10. Magnitude of the transmission coefficient (s_{21}) of the backward wave MLW.

introduced between two feeding waveguides (with a cross-section of 45 mm × 15 mm, and a cut-off frequency of 3.3 GHz), and directly connected with the feeding waveguides. The walls of both the feeding waveguides and the MLW are made of perfectly electrical conductor (PEC). The input and output ports are set up as waveguide ports, which represent a special kind of boundary condition of the computation window, enabling a considerably adapted wave excitation as well as the absorption of energy. In principle this kind of port mimicks an infinitely long waveguide that is connected to the structure. In this case, the waveguide modes leave the structure (and hence the computational domain) toward the boundary planes with very low levels of reflections. In the simulation, the MLW has a length of 60 mm and is loaded with an array of ten MSRRs.

The simulated transmission coefficient (s_{21}) of the MLW is depicted in Fig. 10 [solid line], where the spectral response displays a narrow passband near 8.35 GHz. The cut-off frequency of the waveguide is lowered from 12.5 GHz to about 10.2 GHz because of the CuClad substrate with a relative permittivity of 2.6. It is worth mentioning that the MLW shown in Fig. 2 was experimentally investigated in [4] and the obtained results were further discussed in [24], [44]. From the experimental results one can identify a propagation band around 7.9 GHz, which is close to our simulated result of 8.35 GHz. However, for this below-cut-off (sub-wavelength) passband, there is a large difference between the experimental insertion loss of 30 dB in [4] and our simulated value of 10 dB as shown in Fig. 10. Two reasons mainly contribute to the difference. On one hand, the loss of the CuClad substrate is not considered in the simulation. At resonance, a significant amount of electromagnetic field extends outside the metallic strips and dissipates in the substrate. Therefore, the dielectric loss of the substrate has a significant influence on the insertion loss within this below-cut-off propagation

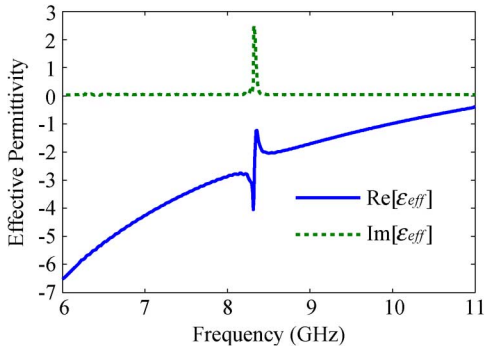

Fig. 11. Extracted real and imaginary parts of the effective permittivity of the backward wave MLW. The solid line represents the real part while the dashed line represents the imaginary part.

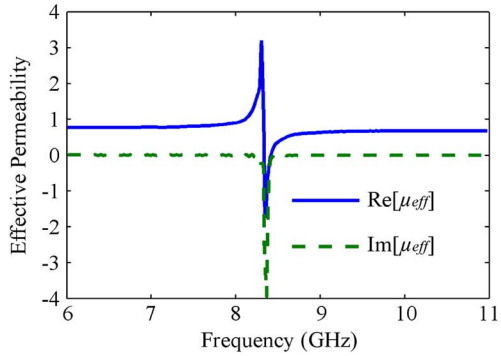

Fig. 12. Extracted real and imaginary parts of the effective permeability of the backward wave MLW. The solid line represents the real part while the dashed line represents the imaginary part.

band. The dashed line in Fig. 10 shows the simulated magnitude of s_{21} for the backward wave MLW with a lossy CuClad substrate, which has dielectric loss tangent of 0.002. It is now confirmed that in this case the simulated insertion loss within the below-cut-off propagation band increases to a value around 23 dB, which is closer to the experimental result. On the other hand, it is hard to accurately simulate the very thin copper cladding of the MSSR, due to the need of a high resolution in the computational mesh that should be fine enough to accommodate the very short penetration length. In this case, down scaling of the copper conductivity in order to cope with the artificial cladding thickness that is dictated by the minimum mesh size should lead to more accurate simulation results. When both, the lossy CuClad substrate and the metallic cladding with smaller conductivity $\sigma = 2 \cdot 10^7$ S/m [i.e. a third of the Copper conductivity] are considered, transmission characteristics of the backward wave MLW are simulated and the magnitude of s_{21} is depicted by the dash-dotted line in Fig. 10. In this case, the insertion loss within the below-cut-off propagation band is around 28 dB and very close to the measured 30 dB. Effective constitutive parameters ε_{eff} and μ_{eff} of the MLW are extracted and the corresponding spectral responses are depicted in Figs. 11 and 12, respectively. The real parts of both the effective permittivity and the effective permeability are simultaneously negative near 8.35 GHz, which means that electromagnetic wave propagation in the MLW appears in the form of backward waves. Worth noticing are the oscillations in the ε_{eff} curves. They arise from the electric response of the MSRR and can be predicted by (13) considering an ε_r in (13) to be equal to the $\varepsilon_{\text{eff}||}$ shown in Fig. 4(b). A similar phenomenon is also present in metamaterials composed of SRRs and thin wires [41].

The dispersion curve for the backward wave MLW [the solid line] is displayed Fig. 13, where the dispersion curve for the MSRRs from Fig. 3(a) is also included [dashed line] for comparison. It can be seen that a passband occurs within the bandgap of the MSRR, and the phase delays as the frequency increases within this passband. From this phenomenon, one can easily underpin the presence of backward waves.

Case B. Forward Wave MLW: When the odd-numbered rods (#1, 3, 5, 7, and 9) in Fig. 2(a) are turned anti-clockwise by 90° and even-numbered rods (#2, 4, 6, 8, and 10) are turned clockwise by 90°, the MLW as shown in Fig. 14 can be realized. In

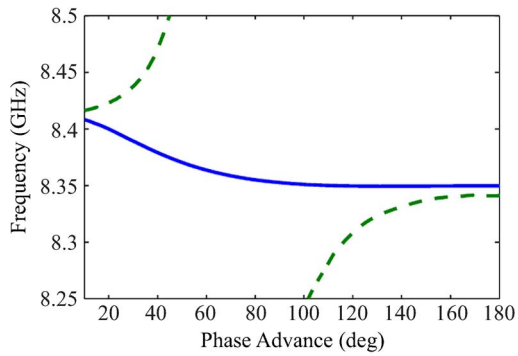

Fig. 13. Dispersion curves for the backward wave MLW and MSRRs only. The solid line corresponds to the backward wave MLW. The dashed line corresponds to the dispersion curve of the MSRRs only [cf. Fig. 3(a)].

this case, the axes of the split rings are parallel to the z-direction, thus the MSRR metamaterial provides negative μ_z and positive μ_x near 8.35 GHz. According to (13) and (14), the MLW will have positive effective permittivity and positive effective permeability to support the propagation of a forward wave near 8.35 GHz. The transmission characteristics of the MLW are simulated using the same system as given in Fig. 9. The length of the simulated forward wave MLW amounts to 60 mm and the underlying waveguide is loaded with an array of ten unit cells to form the MSRR metamaterial.

Fig. 15 depicts the spectral response of the transmission coefficient (s_{21}) for the aforementioned MLW structure. A passband can be identified near 8.35 GHz while the cut-off frequency of the MLW is about 11.5 GHz, which is lower than the cutoff of the corresponding empty waveguide due to the presence of the CuClad substrate. A close inspection of Fig. 10 and Fig. 15 reveals that the cut-off frequencies of backward wave MLWs are smaller compared to the cutoff frequencies of forward wave MLWs. This is due to the specific transversal distribution of the electric field in the waveguide, where e.g. the unperturbed TE_{10} mode yields a single-lobed transversal field profile centered around the waveguide axis so that the influence of the CuClad substrate on the cut-off frequency—namely the detuning towards smaller frequencies—is strongest when the substrate is placed along the center of the waveguide, and is weakest when the substrate is put adjacent to the waveguide walls. For the backward wave MLW, the CuClad substrate is placed along the

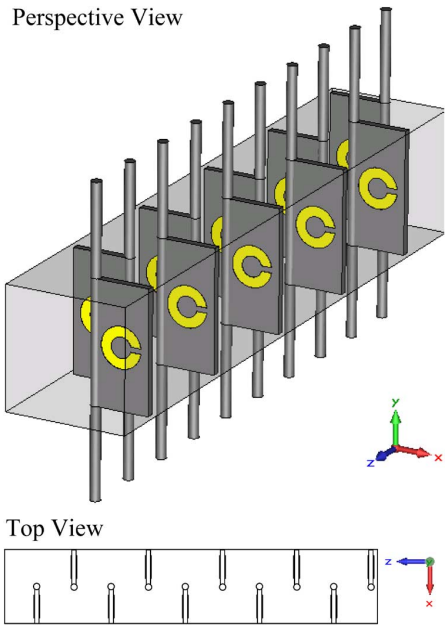

Fig. 14. Geometry of the forward wave MLW.

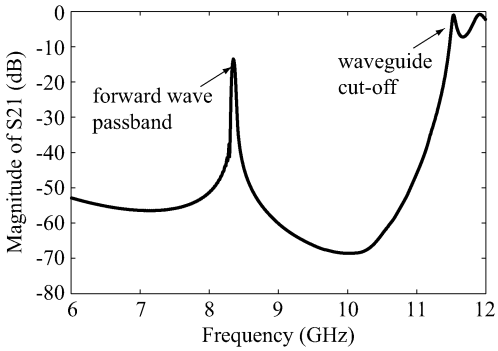

Fig. 15. Magnitude of the transmission coefficient (s_{21}) of the forward wave MLW.

center of the waveguide, whereas for the forward wave MLW, the CuClad substrate extends between the center and the walls of the waveguide, yielding the observed cut-off behavior.

In order to determine the propagating mode for the passband, effective constitutive parameters ε_{eff} and μ_{eff} of the forward wave MLW are extracted and displayed in Figs. 16 and 17, respectively. Both spectral responses confirm that $\text{Re}[\varepsilon_{\text{eff}}]$ and $\text{Re}[\mu_{\text{eff}}]$ are simultaneously positive near 8.35 GHz, underpinning the presence of forward waves in the MLW. Note that outside the resonance region, the value of $\text{Re}[\mu_{\text{eff}}]$ shown in Fig. 17 approaches a value of 0.78 rather than one. According to [45], the physical reason for this inaccuracy is related to the presence of (evanescent) fringe fields at the interface between the MLW (formed by the stack of waveguide sections each containing a MSRR) and the free space, where higher-order modal contributions are expected.

In addition, Figs. 16 and 17 reveal that the spectral response of both $\text{Im}[\mu_{\text{eff}}]$ and $\text{Im}[\varepsilon_{\text{eff}}]$ alternates between positive and negative values. Actually, such imaginary parts with both positive and negative signs have also been observed in [43] and [46]. In particular, the ε_{eff} and μ_{eff} of fishnet-metamaterial in

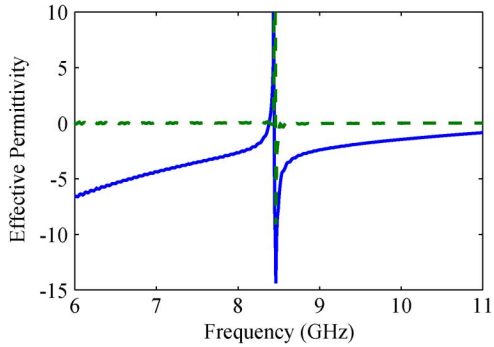

Fig. 16. Extracted real and imaginary parts of the effective permittivity of the forward wave MLW. The solid line represents the real part while the dashed line represents the imaginary part.

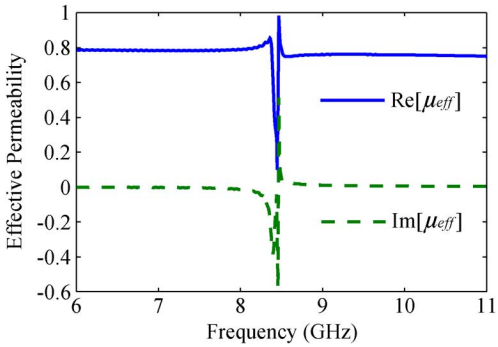

Fig. 17. Extracted real and imaginary parts of the effective permeability of the forward wave MLW. The solid line represents the real part while the dashed line represents the absolute value of the imaginary part.

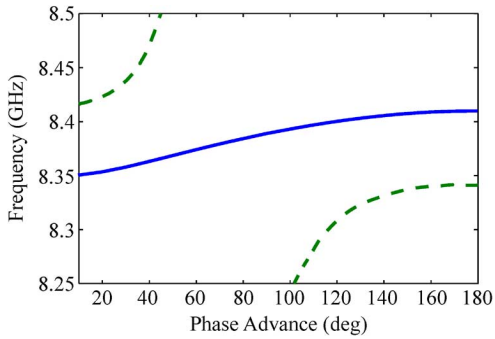

Fig. 18. Dispersion curves for the forward wave MLW and MSRRs only. The solid line corresponds to the forward wave MLW. The dashed line corresponds to the MSRRs only.

[46] and the μ_{eff} of EIT-metamaterial in [43] provide imaginary parts with both signs. Referring to the positive definiteness of the imaginary parts shown in Figs. 4(b) and 5(b), imaginary parts with both signs have a more complicated physical origin. The bipolar range of values is not only caused by the aforementioned radiation loss [refscattered electromagnetic wave], but also related to the exchange of induced electromagnetic energies between the MSRR and the rectangular waveguide [43].

The dispersion curve for the forward wave MLW is calculated and depicted in Fig. 18 [solid line]. For comparison the dispersion curve of the MSRRs from Fig. 3(a) is included as well [dashed line]. The passband occurs within the forbidden band of the MSRR supporting forward waves due to the positive

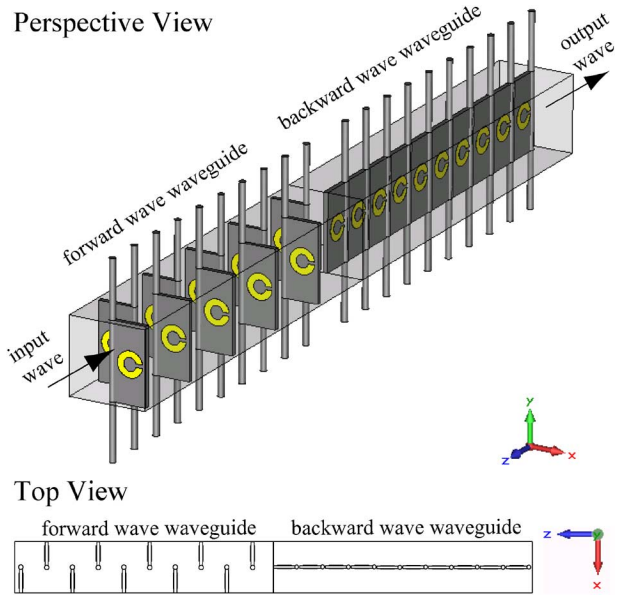

Fig. 19. Geometry of the connected forward wave and backward wave MLWs.

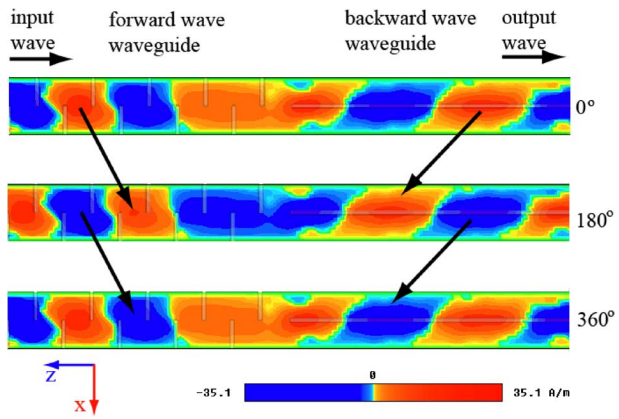

Fig. 20. Snapshots of simulated distributions of the x-component of the magnetic field in the connected MLWs at different time instants at 8.35 GHz.

the slope of the dispersion curve. As a further step the backward wave MLW and the forward wave MLW are connected as shown in Fig. 19, and field distributions in the connected MLWs are computed in order to analyze the propagating modes in the backward wave MLW and the forward wave MLW. The simulation system is similar to that shown in Fig. 9, but the backward MLW is replaced with the connected MLWs. Moreover, the system is excited to get electromagnetic waves propagating from the forward wave MLW to the backward wave MLW. Fig. 20 shows the computed distributions of the x-component of magnetic field at three instants of time corresponding to phase angles of 0°, 180° and 360° at 8.35 GHz. It is clearly observable that the field pattern in the forward wave MLW moves away from the source while the pattern in the backward wave MLW moves toward the source. Hence, forward waves propagate in the forward wave MLW while backward waves propagate in the backward wave MLW. Woth noting is that the electromagnetic energy always propagates forward from the source, irrespective of whether it propagates in the forward wave MLW or in the backward wave

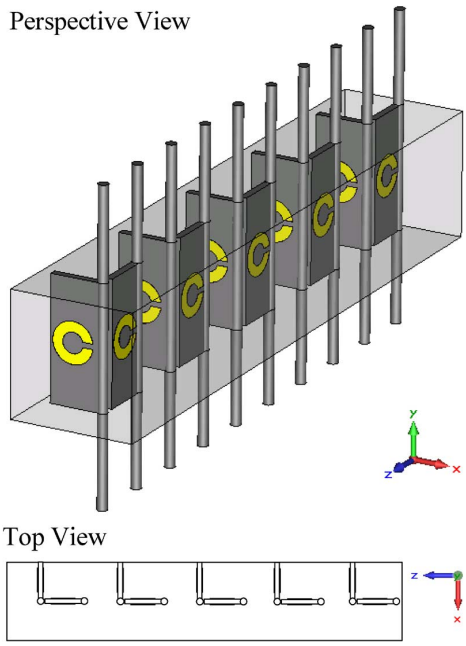

Fig. 21. Geometry of the evanescent wave MLW hosting a 2-D metamaterial.

MLW, because for the forward wave MLW the electromagnetic energy has the same propagation direction with the phase pattern, but for the backward wave MLW the electromagnetic energy and the phase pattern have opposite propagation direction.

Case C. Evanescent Wave MLW: When the odd-numbered rods (#1, 3, 5, 7, and 9) in Fig. 2(a) are turned clockwise by 90° and the even-numbered rods (#2, 4, 6, 8, and 10) are kept unchanged, the evanescent wave MLW as shown in Fig. 21 can be realized. In this case, the loading metamaterial is two-dimensional (2-D) and isotropic, and has negative $\mu_x = \mu_z = \mu_{\text{eff}||}$ near 8.35 GHz. According to (13), the MLW will have positive effective permittivity and negative effective permeability which make the passbands near 8.35 GHz in Fig. 10 and Fig. 15 disappear.

The transmission coefficient (s_{21}) of the evanescent MLW is simulated and depicted in Fig. 22. Comparing the displayed spectral response with the ones in Figs. 10 and 15 indicates an increase of the insertion loss from 10 dB to 30 dB within the propagation band below the cut-off. In addition, the cut-off frequency of the evanescent wave MLW is about 11 GHz, which is higher than the cut-off frequency 10.2 GHz of the backward wave MLW but still lower than the cut-off frequency 11.5 GHz of the forward wave MLW. This also conforms to the layout of the evanescent wave MLW from Fig. 21, where half of the CuClad substrate is placed along the center of the waveguide and the other half is located between the center and the waveguide walls. Hence, the impact of the CuClad substrate on the cut-off frequency for the evanescent wave MLW lies between those for the backward wave MLW and the forward wave MLW.

Both effective permittivity ε_{eff} and effective permeability μ_{eff} of the evanescent MLW are extracted and illustrated in Figs. 23 and 24, respectively. Near 8.4 GHz the spectral response of $\text{Re}[\varepsilon_{\text{eff}}]$ increases from negative to positive values, whereas the magnitude of $\text{Re}[\mu_{\text{eff}}]$ decreases from positive

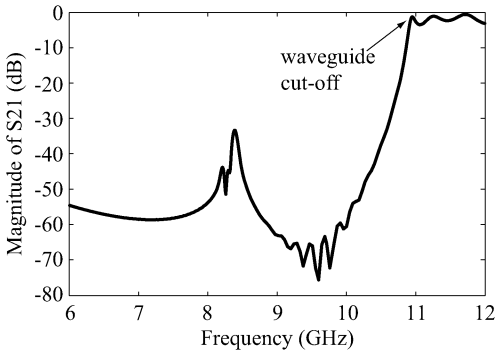

Fig. 22. Magnitude of the transmission coefficient (s_{21}) of the evanescent wave MLW.

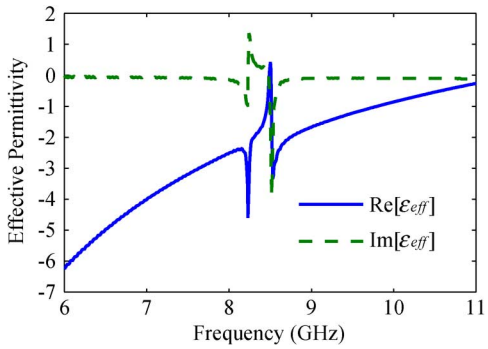

Fig. 23. Extracted real and imaginary parts of the effective permittivity of the evanescent wave MLW. The solid line represents the real part while the dashed line represents the imaginary part.

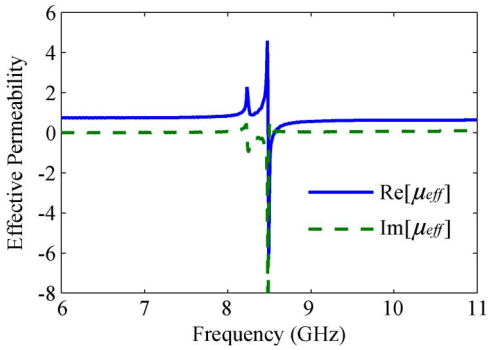

Fig. 24. Extracted real and imaginary parts of the effective permeability of the evanescent wave MLW. The solid line represents the real part while the dashed line represents the imaginary part.

to negative values because of a sharp resonance. The results correspond to the suppressed propagation shown in Fig. 22.

The above results infer that the simulated electromagnetic characteristics correspond to those predicted theoretically, confirming both the theory proposed in Section II and the controllability of MLWs.

V. Impact of Control Rods

In this section, the effect of the control rods on electromagnetic characteristics of the MLW is investigated. In order to reduce a possible impact of the control rods on the overall performance, they should be better made of a non-metallic material that is then characterized with the relative permittivity ε_r.

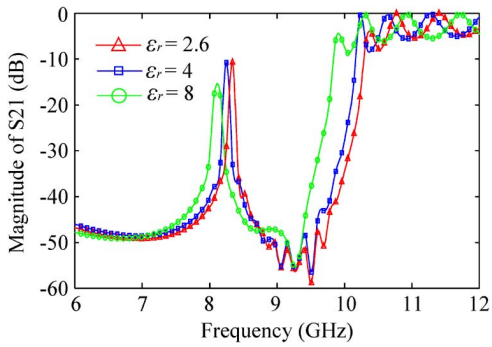

Fig. 25. Effects of control rods with different ε_r on the magnitude of the transmission coefficient of the backward wave MLW when the rods diameter is 1.0 mm.

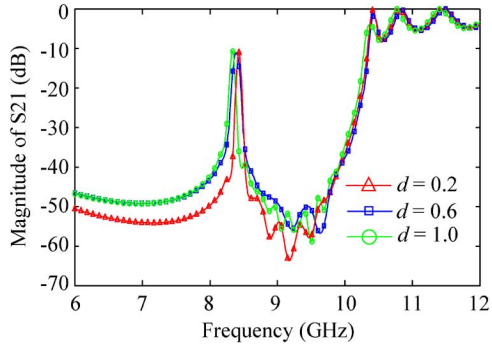

Fig. 26. Effects of control rods with different diameters on the magnitude of the transmission coefficient of the backward wave MLW when $\varepsilon_r = 2.6$.

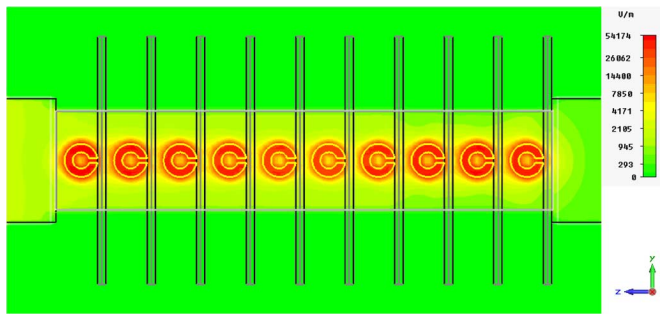

Fig. 27. Intensity distribution of electric field strength within the backward wave MLWat 8.35 GHz.

Therefore, one just has to determine the effects of the relative permittivity and the diameter of control rods.

Figs. 25 and 26 provide an overview of these effects where Fig. 25 shows the influence of the material on the performance of the backward MLW for a rod diameter of 1 mm. The introduction of dielectric control rods into the simulation model slightly decreases the center frequency of the passband in the MLW. This redshift of the passband is further pronounced with increasing relative permittivity of the rods. Fig. 26 shows the impact of diameter changes of the control rods in the backward MLW while keeping $\varepsilon_r = 2.6$. As the diameter increases, the center frequency of the passband slightly decreases. This effect is also very small. Fig. 27 depicts the intensity distribution of the electric field strength within the fully equipped backward wave MLW. The figure also shows that the electric field aggregates

around the MSRRs with virtually now radiation leakage from the MLW through the holes on the walls.

The impact of the control rods on the performance of the forward wave MLW are studied too, and turned out to be comparable to the previous case of the backward wave MLW.

VI. Conclusion

In this paper, a theoretical model for rectangular waveguides loaded by metamaterials was proposed in order to analyze the controllability of the underlying wave propagation, and hence the transmission characteristics of the waveguide system. Numerical simulations were carried out to verify both the proposed theory and the controllability, and the results have proven to be quite accurate. The controllability of the MLWs was enabled using axially rotating control rods that allow the waves in the MLWs to switch from backward to forward propagation or to an evanescent decay. The theory about controllable waveguides loaded by metamaterials and the implementation method of the controllability proposed in this paper are of great practical interest especially in the context of functional MLW devices.

Acknowledgment

The authors would like to thank Prof. W. Hong for very fruitful discussions.

References

[1] G. W. Slade, L. Carin, Q. Xu, S. E. Borchardt, and K. J. Webb, "A study of slotline leaky-wave antennas," *IEEE Trans. Antennas Propag.*, vol. 38, pp. 411–414, 1990.

[2] R. Marques, J. Martel, F. Mesa, and F. Medina, "Left-handed-media simulation and transmission of EM waves in subwavelength split-ring-resonator-loaded metallic waveguides," *Phys. Rev. Lett.*, vol. 89, p. 183901(4), 2002.

[3] R. Marques, J. Martel, F. Mesa, and F. Medina, "A new 2D isotropic left-handed metamaterial design: Theory and experiment," *Microw. Opt. Technol. Lett.*, vol. 35, pp. 405–408, 2002.

[4] S. Hrabar, J. Bartolic, and Z. Sipus, "Waveguide miniaturization using uniaxial negative permeability metamaterial," *IEEE Trans. Antennas Propag.*, vol. 53, pp. 110–119, 2005.

[5] S. Hrabar and D. Zaluski, "Subwavelength guiding of electromagnetic energy in waveguide filled with anisotropic mu-negative metamaterial," *Electromagnetics*, vol. 28, pp. 494–512, 2008.

[6] S. Hrabar and G. Jankovic, "Basic radiation properties of waveguides filled with uniaxial single-negative metamaterials," *Microw. Opt. Technol. Lett.*, vol. 48, pp. 2587–2591, 2006.

[7] M. W. Feise, J. B. Schneider, and P. J. Bevelacqua, "Finite-difference and pseudospectral time-domain methods applied to backward-wave metamaterials," *IEEE Trans. Antennas Propag.*, vol. 52, pp. 2955–2962, 2004.

[8] R. Marques, F. Mesa, J. Martel, and F. Medina, "Comparative analysis of edge- and broadside-coupled split ring resonators for metamaterial design—Theory and experiments," *IEEE Trans. Antennas Propag.*, vol. 51, pp. 2572–2581, 2003.

[9] P. Markos and C. M. Soukoulis, "Numerical studies of left-handed materials and arrays of split ring resonators," *Phys. Rev. E*, vol. 65, p. 36622(8), 2002.

[10] J. B. Pendry, A. J. Holden, D. J. Robbins, and W. J. Stewart, "Magnetism from conductors and enhanced nonlinear phenomena," *IEEE Trans. Microw. Theory Tech.*, vol. 47, pp. 2075–2084, Nov. 1999.

[11] J. D. Baena, J. Bonache, F. Martin, R. M. Sillero, F. Falcone, T. Lopetegi, M. A. G. Laso, J. Garcia-Garcia, I. Gil, M. F. Portillo, and M. Sorolla, "Equivalent-circuit models for split-ring resonators and complementary split-ring resonators coupled to planar transmission lines," *IEEE Trans. Microw. Theory Tech.*, vol. 53, pp. 1451–1460, 2005.

[12] D. R. Smith, W. J. Padilla, D. C. Vier, S. C. Nemat-Nasser, and S. Schultz, "Composite medium with simultaneously negative permeability and permittivity," *Phys. Rev. Lett.*, vol. 84, pp. 4184–4187, May 2000.

[13] R. A. Shelby, D. R. Smith, and S. Schultz, "Experimental verification of a negative index of refraction," *Science*, vol. 292, pp. 77–79, Apr. 2001.

[14] R. A. Shelby, D. R. Smith, S. C. Nemat-Nasser, and S. Schultz, "Microwave transmission through a two-dimensional, isotropic, left-handed metamaterial," *Appl. Phys. Lett.*, vol. 78, pp. 489–491, 2001.

[15] B. Ivsic, Z. Sipus, and S. Hrabar, "Analysis of uniaxial multilayer cylinders used for invisible cloak realization," *IEEE Trans. Antennas Propag.*, vol. 57, pp. 1521–1527, 2009.

[16] S. Hrabar, D. Bonefacic, and D. Muha, "Numerical and experimental investigation of basic properties of wire medium-based shortened horn antennas," *Microw. Opt. Technol. Lett.*, vol. 51, pp. 2748–2753, 2009.

[17] D. Bonefacic, S. Hrabar, and D. Kvakan, "Experimental investigation of radiation properties of an antenna embedded in low permittivity thin-wire-based metamaterial," *Microw. Opt. Technol. Lett.*, vol. 48, pp. 2581–2586, 2006.

[18] G. Lubkowski, C. Damm, B. Bandlow, R. Schuhmann, M. S. ßler, and T. Weiland, "Broadband transmission below the cutoff frequency of a waveguide loaded with resonant scatterer arrays," *IET Microw., Antennas Propag.*, vol. 1, pp. 165–169, 2007.

[19] A. Alu and N. Engheta, "Guided modes in a waveguide filled with a pair of single-negative (SNG), double-negative (DNG), and/or double-positive (DPS) layers," *IEEE Trans. Microw. Theory Tech.*, vol. 52, pp. 199–210, 2004.

[20] S. Antipov, L. Spentzouris, W. Gai, M. Conde, F. Franchini, R. Konecny, W. Liu, J. G. Power, Z. Yusof, and C. Jing, "Observation of Wakefield generation in left-handed band of metamaterial-loaded waveguide," *J. Appl. Phys.*, vol. 104, p. 014901(6), 2008.

[21] J. D. Baena, L. Jelinek, and R. Marques, "Reducing losses and dispersion effects in multilayer metamaterial tunnelling devices," *New J. Phys.*, vol. 7, p. 166(13), 2005.

[22] H. Bahrami, M. Hakkak, and A. Pirhadi, "Analysis and design of highly compact bandpass waveguide filter utilizing Complementary Split Ring Resonators (CSRR)," *Progr. Electromagn. Res.*, vol. 80, pp. 107–122, 2008.

[23] H. Xu, Z. Wang, J. Hao, J. Dai, L. Ran, J. A. Kong, and L. Zhou, "Effective-medium models and experiments for extraordinary transmission in metamaterial-loaded waveguides," *Appl. Phys, Lett.*, vol. 92, p. 041122(3), 2008.

[24] S. Hrabar, J. Bartolic, and Z. Sipus, "Reply to "Comments on waveguide miniaturization using uniaxial negative permeability metamaterial"," *IEEE Trans. Antennas Propag.*, vol. 55, pp. 1017–1018, 2007.

[25] J.-C. Liu, C.-Y. Liu, Y.-S. Hong, C.-Y. Wu, and D.-C. Lou, "Waveguide miniaturization with SR(ZNTI)FE10O19 hexaferrite metamaterial," *Microw. Opt. Technol. Lett.*, vol. 49, pp. 201–203, 2007.

[26] I. A. Eshrah and A. A. Kishk, "Electric-type dyadic Green's functions for a corrugated rectangular metaguide based on asymptotic boundary conditions," *IEEE Trans. Antennas Propag.*, vol. 55, pp. 355–363, 2007.

[27] I. A. Eshrah and A. A. Kishk, "Magnetic-type dyadic Green's functions for a corrugated rectangular metaguide based on asymptotic boundary conditions," *IEEE Trans. Microw. Theory Tech.*, vol. 55, pp. 1124–1131, 2007.

[28] I. A. Eshrah, A. A. Kishk, A. B. Yakovlev, and A. W. Glisson, "Spectral analysis of left-handed rectangular waveguides with dielectric-filled corrugations," *IEEE Trans. Antennas Propag.*, vol. 53, pp. 3673–3683, 2005.

[29] I. A. Eshrah, A. A. Kishk, A. B. Yakovlev, and A. W. Glisson, "Rectangular waveguide with dielectric-filled corrugations supporting backward waves," *IEEE Trans. Microw. Theory Tech.*, vol. 53, pp. 3298–3304, 2005.

[30] F. Y. Meng, Q. Wu, J. H. Fu, X. M. Gu, and L. W. Li, "An anisotropic metamaterial-based rectangular resonant cavity," *Appl. Phys, A*, vol. 91, pp. 573–578, 2008.

[31] J. Carbonell, L. J. Rogla, V. E. Boria, and D. Lippens, "Design and experimental verification of backward-wave propagation in periodic waveguide structures," *IEEE Trans. Microw. Theory Tech.*, vol. 54, pp. 1527–1532, 2006.

[32] A. M. Attiya, A. A. Kishk, and A. W. Glisson, "Analysis of two-dimensional magneto-dielectric grating slab," *Progr. Electromagn. Res.*, vol. 74, pp. 195–216, 2007.

[33] P. A. Belov and C. R. Simovski, "Subwavelength metallic waveguides loaded by uniaxial resonant scatterers," *Phys. Rev. E*, vol. 72, p. 036618(11), 2005.
[34] A. Alu, F. Bilotti, N. Engheta, and L. Vegni, "Theory and simulations of a conformal omni-directional subwavelength metamaterial leaky-wave antenna," *IEEE Trans. Antennas Propag.*, vol. 55, pp. 1698–1708, 2007.
[35] F. P. Casares-Miranda, C. Camacho-Penalosa, and C. Caloz, "High-gain active composite right/left-handed leaky-wave antenna," *IEEE Trans. Antennas Propag.*, vol. 54, pp. 2292–2300, 2006.
[36] T. Ueda, K. Horikawa, M. Akiyama, and M. Tsutsumi, "Nonreciprocal phase-shift composite right/left handed transmission lines and their application to leaky wave antennas," *IEEE Trans. Antennas Propag.*, vol. 57, pp. 1995–2005, 2009.
[37] T. Ueda, N. Michishita, M. Akiyama, and T. Itoh, "Dielectric-resonator-based composite right/left-handed transmission lines and their application to leaky wave antenna," *IEEE Trans. Microw. Theory Tech.*, vol. 56, pp. 2259–2269, 2008.
[38] R. Marques, F. Medina, and R. Rafii-El-Idrissi, "Role of bianisotropy in negative permeability and left-handed metamaterials," *Phys. Rev. B*, vol. 65, p. 144440(6), 2002.
[39] R. W. Ziolkowski, "Design, fabrication, and testing of double negative metamaterials," *IEEE Trans. Antennas Propag.*, vol. 51, pp. 1516–1529, 2003.
[40] D. R. Smith, D. C. Vier, T. Koschny, and C. M. Soukoulis, "Electromagnetic parameter retrieval from inhomogeneous metamaterials," *Phys. Rev. E*, vol. 71, p. 036617(11), 2005.
[41] D. R. Smith, S. Schultz, P. Markos, and C. M. Soukoulis, "Determination of effective permittivity and permeability of metamaterials from reflection and transmission coefficients," *Phys. Rev. B*, vol. 65, p. 195104(5), 2002.
[42] A. F. Starr, P. M. Rye, D. R. Smith, and S. Nemat-Nasser, "Fabrication and characterization of a negative-refractive-index composite metamaterial," *Phys. Review B*, vol. 70, p. 113102(4), 2004.
[43] K. L. Tsakmakidis, M. S. Wartak, J. J. H. Cook, J. M. Hamm, and O. Hess, "Negative-permeability electromagnetically induced transparent and magnetically active metamaterials," *Phys. Rev. A*, vol. 81, p. 195128(11), 2010.
[44] F.-Y. Meng, Q. Wu, B.-S. Jin, H.-L. Wang, and J. Wu, "Comment on 'Waveguide miniaturization using uniaxial negative permeability metamaterial'," *IEEE Trans. Antennas Propag.*, vol. 55, pp. 1016–1017, 2007.
[45] M. G. Silveirinha, A. Alu, and N. Engheta, "Parallel-plate metamaterials for cloaking structures," *Phys. Rev. E*, vol. 75, p. 036603(16), 2007.
[46] N. Liu, L. Fu, S. Kaiser, H. Schweizer, and H. Giessen, "Plasmonic building blocks for magnetic molecules in three-dimensional optical metamaterials," *Adv. Mater.*, vol. 20, pp. 3859–3865, 2008.

Fan-Yi Meng (M'07) received the B.S., M.S., and Ph.D. degrees in electromagnetics from Harbin Institute of Technology, Harbin, China, in 2002, 2004 and 2007, respectively.

Since Aug. 2007, he has been with the Department of Microwave Engineering at the Harbin Institute of Technology where he is currently an Assistant Professor. He has (co-)authored 3 books, 30 international refereed journal papers, over 20 regional refereed journal papers, and 20 international conference papers. His current research interests include electromagnetic and optical metamaterials, plasmonics, and EMC.

Dr. Meng was the recipient of a number of awards including the 2010 Award of Science and Technology from the Heilongjiang Province Government of China, the 2010 "Microsoft Cup" IEEE China Student Paper Contest Award, two best paper awards from the National Conference on Microwave and Millimeter Wave in China, in 2009 and 2007, respectively, the Young Scientist Travel Grant (YSTG) from the International Symposium on Antennas and Propagation in Japan, in 2007, the 2007 Excellent Graduate Award of Heilongjiang Province of China, and the Outstanding Doctor Degree Dissertation Award of Harbin Institute of Technology.

Qun Wu (SM'05) received the B.Sc. degree in radio engineering, thr M.Eng. degree in electromagnetic fields and microwave technology, and the Ph.D. degree in communication and information systems engineering, all at Harbin Institute of Technology (HIT), Harbin, China, in 1977, 1988, and 1999, respectively.

He worked as a Visiting Professor at Seoul National University (SNU), Korea, from 1998 to 1999, and Pohang University of Science and Technology, from 1999 to 2000. Since 1990, he has been with Department of Electronic and communication Engineering at HIT, China, where he is currently a Professor. He has published over 30 international and regional refereed journal papers. His current research interests are in microwave active circuits, electromagnetic compatibility, MMIC, and millimeterwave MEMS devices.

Dr. Wu received two Third-Class Prizes and one Second-Class Prize of Scientific Progress Awards from the Ministry of Aerospace of China in 1989 and 1992, respectively.

Daniel Erni (S'88–M'93) received the diploma degree in electrical engineering from the University of Applied Sciences, Rapperswil (HSR), Switzerland, in 1986 and the diploma degree in electrical engineering and the Ph.D. degree from ETH Zürich, Zürich Switzerland, in 1990 and 1996, respectively.

Since 1990, he has been working at the Laboratory for Electromagnetic Fields and Microwave Electronics, ETH Zürich. From 1995 to 2006, he was the Founder and head of the Communication Photonics Group, ETH Zürich. Since Oct. 2006, he is a Full Professor for General and Theoretical Electrical Engineering at the University of Duisburg-Essen, Germany (http://www.ate.uni-due.de/). His current research includes advanced data transmission schemes (i.e. O-MIMO) in board-level optical interconnects, optical on-chip interconnects, ultra-dense integrated optics, nanophotonics, plasmonics, electromagnetic and optical metamaterials, and quantum optics. On the system level he has pioneered the introduction of numerical structural optimization into dense integrated optics device design. He is a member of the editorial board of the *Journal of Computational and Theoretical Nanoscience* and edited the 2009 Special Issue on Functional Nanophotonics and Nanoelectromagnetics.

Dr. Erni is a Fellow of the Electromagnetics Academy, a member of the Center for Nanointegration Duisburg-Essen (CeNIDE), an associate member of the Swiss Electromagnetics Research Centre (serec), as well as a member of the Swiss Physical Society (SPS), the German Physical Society (DPG), and of the Optical Society of America (OSA).

Le-Wei Li (F'10) received the B.Sc. degree in physics from Xuzhou Normal University (XNU), Xuzhou, China, in 1984, the M.Eng.Sc. degree in electrical engineering from China Research Institute of Radiowave Propagation (CRIRP), Xinxiang, China, in 1987, and the Ph.D. degree in electrical engineering from Monash University, Melbourne, Australia, in 1992.

Since 1992, he has been with the Department of Electrical & Computer Engineering, National University of Singapore, where he is currently a Professor and the Director of NUS Centre for Microwave and Radio Frequency. From 1999 to 2004, he was seconded to the High Performance Computations on Engineered Systems (HPCES) Programme of Singapore-MIT Alliance (SMA) as an SMA Faculty Fellow. His current research interests include electromagnetic theory, computational electromagnetics, radio wave propagation and scattering in various media, microwave propagation and scattering in tropical environment, and analysis and design of various antennas. In these areas, he has (co-)authored 3 books, 45 book chapters, over 280 international refereed journal papers, 31 regional refereed journal papers, and over 320 international conference papers.